Magnetotransport and electronic structure of EuAuSb: A candidate antiferromagnetic Dirac semimetal

D. Ram,[1] J. Singh,[2] S. Banerjee,[3] A. Sundaresan,[3] D. Samal,[4] V. Kanchana,[2,*] and Z. Hossain[1,†]

[1]*Department of Physics, Indian Institute of Technology, Kanpur 208016, India*

[2]*Department of Physics, Indian Institute of Technology Hyderabad, Kandi, Sangareddy 502 285, Telangana, India*

[3]*School of Advanced Materials, and Chemistry and Physics of Materials Unit, Jawaharlal Nehru Centre for Advanced Scientific Research, Jakkur, Bangalore 560064, India*

[4]*Institute of Physics, Bhubaneswar 751005, India*[‡]

(Received 18 November 2023; revised 24 February 2024; accepted 22 March 2024; published 18 April 2024)

We have investigated the magnetic, thermodynamic, and electrical transport properties of EuAuSb single crystals as well as carrying out band structure calculations. The powder x-ray diffraction data confirm that EuAuSb crystallizes in ZrBeSi-type hexagonal structure with space group $P6_3/mmc$. The magnetic measurements reveal an antiferromagnetic (AFM) ordering in EuAuSb at $T_N = 3.3$ K. This transition is further confirmed by heat capacity and electrical resistivity data. The isothermal magnetization data saturate at low magnetic field of $\mu_0 H_s^c = 2.9$ and $\mu_0 H_s^{ab} = 3.8$ T for $H \perp c$ and $H \parallel c$, respectively, while the magnetization along $H \perp c$ displays a metamagnetic transition around $\mu_0 H_m^{ab} = 0.95$ T. The electrical resistivity exhibits a metallic behavior down to 35 K; after that it shows an upturn until T_N due to the influence of short-range interactions. The longitudinal and transverse magnetoresistances of EuAuSb are negative ($\sim -45\%$ and -42% in 10 T at 2 K, respectively); in the high field at $T \leqslant 40$ K, they switch to a positive value above 40 K. Further, we observe a humplike anomaly in the Hall resistivity [$\rho_{xy}(H)$] data below T_N, which is most likely a manifestation of the topological Hall effect. Our two-band model analysis of $\rho_{xy}(H)$ data indicates both hole and electron charge carriers contribute to the electrical transport of the compound. The electronic band structure calculations reveal a Γ-centered nodal line in the absence of spin-orbit coupling (SOC). In the presence of SOC, the compound hosts the Dirac point. The Z_2 invariants, in the presence of effective time-reversal and inversion symmetries, categorize this system as a nontrivial topological material. Our combined experimental and theoretical studies suggest EuAuSb to be a potential AFM topological semimetal.

DOI: 10.1103/PhysRevB.109.155152

I. INTRODUCTION

Magnetic topological semimetals play a significant role in understanding the interplay between magnetism and exotic relativistic fermions [1–6]. These materials have extraordinary magnetotransport properties such as the anomalous Hall effect (AHE) [7–9], topological Hall effect (THE) [4–6], and topological Nernst effect [10,11], which are easily tunable by changing their Fermi level with respect to Dirac/Weyl points using magnetic field and chemical doping [12–15]. Furthermore, these materials also exhibit interesting quantum phenomena like quantum AHE [16–18] and axion electrodynamics [19–21]. Especially, Eu-based magnetic topological materials have drawn more attention as they have various magnetic ground states, a quenched orbital momentum, no crystalline electric field, and extremely weak spin-orbit coupling (SOC) due to the electron configuration $4f^7$ of Eu^{2+} with a half-filled f shell. These compounds provide an ideal platform for investigating the interplay between magnetism and topology [22–26]. For example, $EuBiTe_3$ is a topological insulator with antiferromagnetic (AFM) ordering; it shows negative magnetoresistance (MR) and crossover between weak antilocalization (WAL) and weak localization due to the presence of magnetic polarons [27]. The magnetic ordering of $EuCd_2As_2$ depends on the level of band filling [25]. Antiferromagnet $EuMnBi_2$ exhibits the half-integer quantum Hall effect [26]. Further, the field-induced topological phases were observed in many Eu-based compounds such as $EuAs_3$ [28] and EuP_3 [29].

Recently, many compounds of the EuTX (where T = Cu, Ag, and Au; X = pnictides) family were proposed to host topological Dirac semimetals through electronic band structure calculations and experiment results [4,14,30–32]. These compounds possess a ZrBeSi-type hexagonal structure with a space group $P6_3/mmc$ (D_{6h}^4) [14]. For instance, the Dirac semimetal EuAgAs exhibits a large THE with an AFM ground state. On the other hand, superconductivity with multiple magnetic transitions and strong Rashba-type spin-orbit interaction are observed in semimetal EuAuBi [32]. These interesting results motivated us to explore further the crystal growth and physical properties of a new member of the EuTX family (i.e., EuAuSb). We have grown EuAuSb single crystals using bismuth flux. Magnetic susceptibility measurements exhibit an AFM ordering at $T_N = 3.3$ K, followed by heat

*kanchana@iith.ac.in

†zakir@iitk.ac.in

‡The Institute of Physics at Bhubaneswar is a constituent institution of Homi Bhabha National Institute, India.

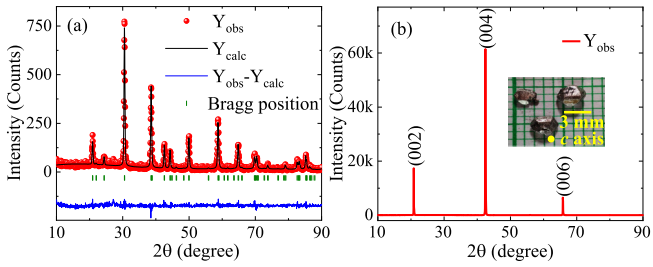

FIG. 1. (a) The powder XRD pattern of crushed single crystals of EuAuSb was recorded at room temperature. The observed and calculated intensities are represented by red circles and solid black line, respectively. A solid blue line presents the difference between observed and calculated intensities. Olive tick marks are Bragg peak positions. (b) The single-crystal XRD pattern of EuAuSb. The inset shows an optical image of single crystals.

capacity and electrical resistivity data. The longitudinal and transverse magnetoresistance of EuAuSb show a maximum negative value around T_N in high fields. Interestingly, the Hall resistivity data reveal a broad hump below T_N and both charge carries are present in electrical transport of EuAuSb. Our results reveal that EuAuSb is a Dirac semimetal with AFM ground state and anomalous transport properties.

II. EXPERIMENTAL DETAILS

Single crystals of EuAuSb were grown using bismuth as an external flux. Starting elements Eu (99.9%), Au (99.99%), Sb (99.999%), and Bi (99.999%) from Alfa Aesar were taken in a molar ratio of 1:1:1:9. All elements were mixed properly in an alumina crucible and sealed inside a quartz tube under partial argon gas atmosphere. Next, the whole assembly was heated to 1050 °C and held for 24 h. The assembly was slowly cooled down to 600 °C at a rate of 3 °C/h. At this temperature, the assembly was removed from the furnace and centrifuged. Shiny hexagonal-like plate crystals with typical dimensions $2\times2\times0.5$ mm^3 were obtained, as shown in the inset of Fig. 1(b).

The crystal structure and orientation of grown single crystals were checked by x-ray diffraction (XRD) on a PANalytical X'Pert PRO diffractometer with Cu $K_{\alpha1}$ radiation. The chemical composition was determined using energy-dispersive x-ray spectroscopy (EDS) using a JEOL JSM-6010LA scanning electron microscope. The heat capacity measurement was performed by the conventional relaxation method in a Quantum Design physical property measurement system. Magnetic susceptibility and magnetization measurements were conducted down to 2 K using a Quantum Design magnetic property measurement system. Magnetotransport measurements were performed using the Cryogen Free Measurement System from Cryogenic Ltd., equipped with 12 T superconducting magnets, an integrated variable-temperature sample space, and a Lakeshore M81 synchronous source measure unit by the standard four-probe method in ac transport mode. All resistivity and MR measurements were carried out by the electrical current being within the hexagonal *ab* plane of the crystal, while the magnetic field was applied along the crystallographic *c* axis for transverse magnetoresistance (TMR) and Hall resistivity and parallel to the *ab* plane of crystal for longitudinal magnetoresistance (LMR). All MR and Hall resistivity data were performed in positive and negative magnetic fields to rule out the possibility of erroneous resistivity contributions from misaligned of probe contacts. For the magnetoresistivity $\rho_{xx}(H)$, a symmetrization approach was used to eliminate the erroneous transverse contribution, as denoted by the formula $\rho_{xx}(H) = [\rho_{xx}(H) + \rho_{xx}(-H)]/2$. In contrast, an antisymmetrization approach was used to remove the erroneous longitudinal contribution in the case of Hall resistivity $\rho_{xy}(H)$, where $\rho_{xy}(H) = [\rho_{xy}(H) - \rho_{xy}(-H)]/2$.

The electronic structure calculations were performed using density functional theory (DFT) [33,34]. The calculations utilized a plane-wave basis set along with the projector augmented wave method [35], as incorporated in the Vienna *ab* initio simulation package (VASP) [36,37]. The exchange-correlation functional was implemented through the application of the Perdew, Burke, and Ernzerhof (PBE) parametrized generalized gradient approximation (GGA) [38]. To address the substantial correlation effects of Eu-f states, we incorporated an effective Hubbard U parameter (GGA+U) with a value of $U = 7$ eV [39,40]. For all computations, a plane wave energy cutoff of 500 eV was employed, with an energy convergence threshold of 10^{-6} eV. Geometry optimizations were carried out by employing a dense k mesh in accordance with the Monkhorst-Pack method [41]. The WANNIER90 package was used to obtain a tight-binding Hamiltonian based on maximally localized Wannier functions for the surface state calculations [42]. The topological features of the compound were investigated using the iterative Green's function approach, which is implemented in the WANNIERTOOLS package, based on the tight-binding model [43,44].

III. RESULTS AND DISCUSSION

A. Crystal structure

The room-temperature powder XRD pattern of crushed single crystals of EuAuSb is shown in Fig. 1(a). The powder XRD data are analyzed using Rietveld refinement in the FULLPROF software. Our refinement yields the hexagonal structure with space group $P6_3/mmc$ (No. 194) and lattice parameters $a = b = 4.6678$ Å and $c = 8.4976$ Å. These lattice parameters match well with the previously reported values for polycrystalline samples [45–47]. Figure 1(b) displays the XRD pattern measured on a hexagonal-shaped plate single crystal. The presence of (00l) peaks in the diffraction pattern suggests that the platelike surface is oriented perpendicular to the *c* axis. The EDS data are taken at multiple positions and areas on the single crystal show the atomic ratio Eu : Au : Sb $= 1.00 \pm 0.02 : 1.04 \pm 0.02 : 1.03 \pm 0.01$, which is very close to the stoichiometric ratio of EuAuSb.

B. Magnetic properties

Figures 2(a) and 2(b) show temperature-dependent magnetic susceptibility ($\chi = M/H$) at various magnetic fields for parallel and perpendicular to the *c* axis, respectively. The $\chi(T)$ data are taken under zero-field cooled (ZFC) and field-cooled (FC) mode for both field orientations $H \parallel c$ and $H \perp c$,

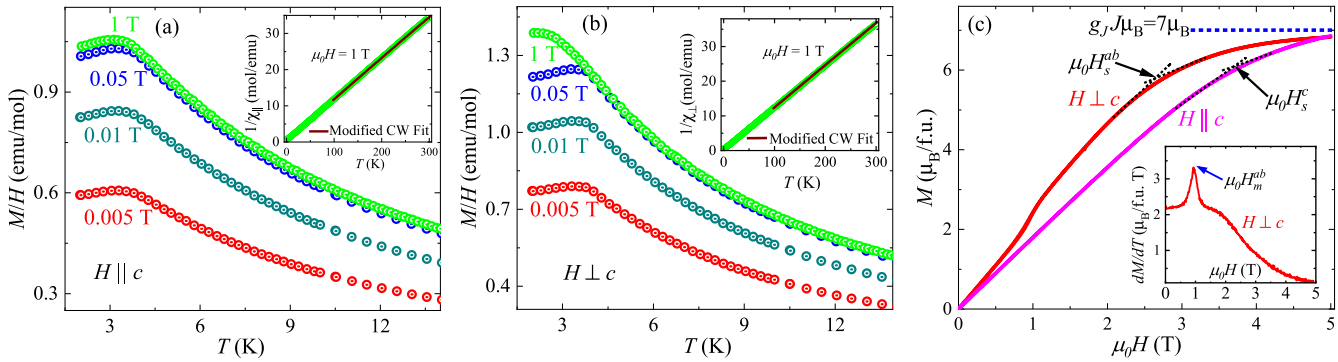

FIG. 2. The temperature-dependent magnetic susceptibility (M/H) measured under various magnetic fields for (a) $H \parallel c$ and (b) $H \perp c$. Insets of (a) and (b) show the inverse magnetic susceptibility as a function of temperature for $H \parallel c$ and $H \perp c$, respectively. The solid brown line represents the Curie-Weiss fit above 100 K. (c) The isothermal magnetization as a function of magnetic field at 2 K for $H \parallel c$ and $H \perp c$. The inset of (c) displays the derivative of magnetization data for $H \perp c$.

which show no difference between ZFC and FC data (here not shown). At $\mu_0 H = 0.005$ T, $\chi(T)$ data for both field orientations clearly show a cusp at $T_N = 3.3$ K, which is close to T_N (=4.1 K) of a polycrystalline sample reported earlier in Ref. [47]. As the magnetic field strength increases from 0.005 to 1 T, the T_N shifts to a lower temperature of 3.0 K; this is a general characteristic of antiferromagnets [48–50]. The inverse magnetic susceptibility $[\chi^{-1}(T)]$ data at $\mu_0 H = 1$ T are plotted as a function of temperature and are shown in insets of Figs. 2(a) and 2(b) for $H \parallel c$ and $H \perp c$, respectively. The $\chi^{-1}(T)$ can be described by the modified Curie-Weiss expression $\chi(T) = \chi_0 + C/(T - \Theta_P)$ in the temperature range 100–300 K, where χ_0 is the temperature-independent magnetic susceptibility, and C and Θ_P are the Curie constant and paramagnetic Curie temperature, respectively. The least-squares fitting yields values of $\Theta_P = -2.1$ and -1.1 K; $\chi_0 = 5.40\times10^{-4}$ and $\chi_0 = 2.56\times10^{-4}$ emu/mol for $H \parallel c$ and $H \perp c$, respectively. The negative values of Θ_P indicate the presence of AFM interactions in the system. The estimated value of effective magnetic moment $\mu_{eff} = 8.28\ \mu_B$/Eu (for $H \parallel c$) and 8.05 μ_B/Eu (for $H \perp c$), which are close to the theoretical value of $g\sqrt{J(J+1)}\ \mu_B = 7.94\ \mu_B$ for the Eu^{2+} ion ($J = 7/2$ and $g_J = 2$).

To have further insight on the magnetic behavior, we have measured the field-dependent isothermal magnetization $M(H)$ at 2 K for $H \parallel c$ and $H \perp c$, as displayed in Fig. 2(c). The $M(H)$ first increases almost linearly with increasing field up to $\mu_0 H_s^c = 3.8$ and $\mu_0 H_s^{ab} = 2.9$ T for $H \parallel c$ and $H \perp c$, respectively. The $M(H)$ starts to saturate at $\mu_0 H_s^c$ and $\mu_0 H_s^{ab}$ with saturation value ~6.84 and 6.82 μ_B/Eu for $H \parallel c$ and $H \perp c$, respectively. These values are very close to the theoretical value $g_J J\ \mu_B = 7\ \mu_B$ for a free Eu^{2+} ion, indicating all spins of Eu^{2+} are aligned along the direction of applied magnetic field. The $M(H)$ data for $H \perp c$ show a small kink at $\mu_0 H_m^{ab} = 0.95$ T [see clear peak in dM/dH vs H curve, as displayed in inset of Fig. 2(c)], which suggests a metamagnetic (MM) transition in the ab plane. However, the MM transition is not observed for $H \parallel c$, suggesting that moments of Eu^{2+} lie in the hexagonal ab plane of crystal with some canting. The overall magnetic behavior of EuAuSb is similar to that observed of isostructural ternary compounds, such as EuCuAs [51], EuAuAs [31], and EuAgAs [4].

C. Heat capacity and entropy

Figure 3 displays the heat capacity C_p of the EuAuSb single crystal measured at constant pressure in the temperature range of 2–50 K. The $C_p(T)$ data show a pronounced λ-shaped peak around $T_N = 3.3$ K, which is confirming the bulk nature of AFM ordering. Further, we have plotted C_p/T as a function of T^2 (see the top inset of Fig. 3), which is fitted using the Debye model $C_{ph}(T) = \gamma T + \beta T^3$ in temperature $8 \leqslant T \leqslant 15$ K, where γ is the Sommerfeld coefficient and β is the coefficient of phonon contribution to heat capacity. The so-obtained parameters are $\gamma = 91(2)$ mJ mol^{-1} K^{-2} and $\beta = 1.53(1)$ mJ mol^{-1} K^{-4}. The Debye temperature Θ_D of ~156 K is derived from β. Such values of γ and Θ_D were also observed in many other Eu-based compounds like EuAuAs [31], $EuBiTe_3$ [27], and EuAgAs [4]. The large value of γ may come from magnon contributions due to the ordering of Eu moments. According to the mean-field theory, the amount of jump at T_N in $C_p(T)$ data can be used to distinguish between two possible magnetic structures: (i) equal moment (EM) at all sites and (ii) periodically varying moments (amplitude

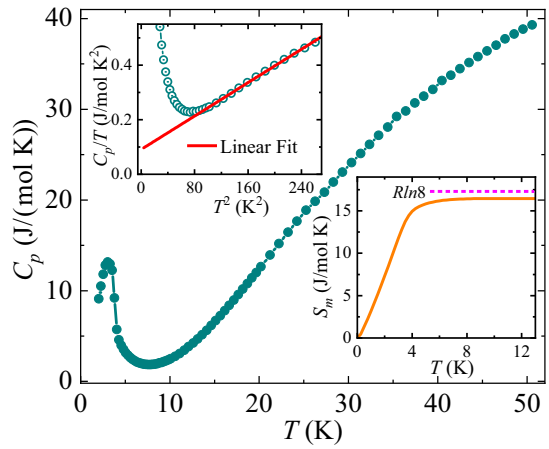

FIG. 3. Temperature-dependent heat capacity (C_p) of EuAuSb single crystal. Top inset shows a plotting of C_p/T vs T^2. The red line fits the expression $C_{ph}/T = \gamma + \beta T^2$. Bottom inset displays the magnetic entropy S_m as a function of temperature.

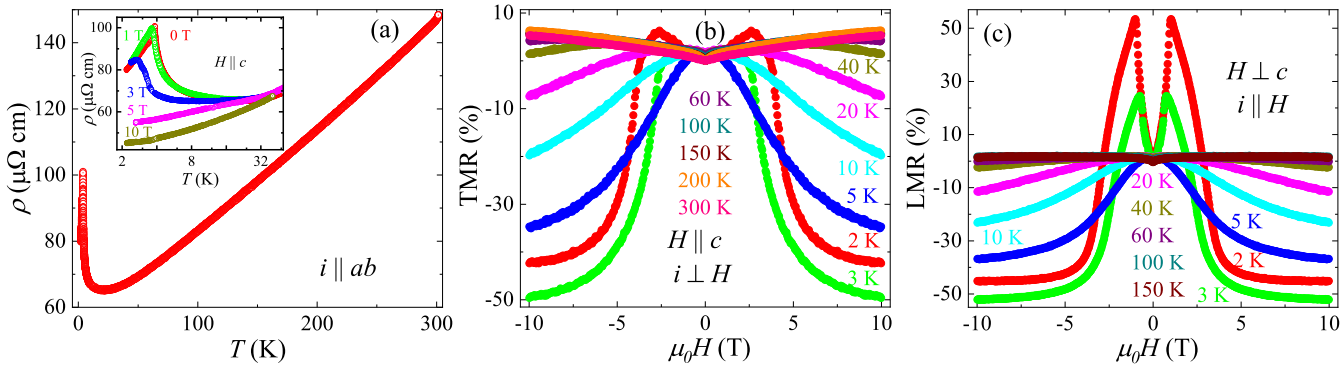

FIG. 4. (a) The temperature-dependent electrical resistivity of EuAuSb single crystal. The inset shows electrical resistivity with various fields up to 10 T. Panels (b) and (c) represent the field-dependent transverse and longitudinal magnetoresistance at selective temperatures, respectively.

modulated, AM). For $J = 7/2$, the amount of jump expected is $\Delta C_{EM} = 20.15$ J/(mol K) and $\Delta C_{AM} = 13.43$ J/(mol K) for EM and AM structure, respectively [52–54]. The amount of jump in $C_p(T)$ is determined using $\Delta C/T_N = (C_p - C_{ph})/T_N$; the obtained value is $\Delta C = 12.84$ J/(mol K). This value is very close to the value of amplitude modulated magnetic structure, suggesting a possible AM structure of EuAuSb. To extract the magnetic heat capacity C_m, we subtracted the lattice contribution C_{ph}, as calculated using $C_{ph} = \gamma T + \beta T^3$. Further, we estimated the magnetic entropy by the expression $S_m = \int \frac{C_m}{T} dT$, as displayed in bottom inset of Fig. 3. The magnetic entropy S_m increases with increasing temperature and saturates at $T = 6$ K. The saturation value of $S_m(T)$ is ∼16.5 J/(mol K), which is about 95% of the theoretical value $R\ln(2J + 1) \approx 17.3$ J/(mol K) for Eu^{2+} ion.

D. Electrical resistivity and magnetoresistance

The temperature-dependent electrical resistivity ρ of the EuAuSb single crystal measured in zero magnetic field is presented in Fig. 4(a). The room-temperature resistivity is a large value (∼148 μΩ cm) from typical metal, which is comparable to the value of a previous polycrystalline report [45] as well as many Eu-based ternary compounds like EuAgAs [4], EuAuAs [31], EuAuBi [32], and $EuIn_2As_2$ [19,55]. The $\rho(T)$ decreases in a metallic manner with decreasing temperature down to 35 K. After that, it starts to increase and shows an upturn due to the influence of short-range interactions and reaches a maximum at $T_N = 3.3$ K, which corroborates with the result of magnetic and heat capacity measurements. In the magnetically ordered state, the $\rho(T)$ sharply decreases due to the reduction of spin-disorder scattering. A similar upturn at low temperature in $\rho(T)$ is also observed in other Eu-based compounds [4,19,31]. Next, we have measured the $\rho(T)$ with selective transverse magnetic fields ($H \parallel c$) up to 10 T, as displayed in the inset of Fig. 4(a). As field strength increases, the peak of T_N shifts towards the lower temperature; it is completely suppressed under magnetic field 5 T. Above 5 T, the $\rho(T)$ smoothly decreases with decreasing temperature; it does not show any upturn down to 2 K.

The isothermal TMR and LMR of the EuAuSb single crystal measured at different temperatures are shown in Figs. 4(b) and 4(c), respectively. The MR is defined as MR (%) = $[\rho(H) - \rho(0)] \times 100/\rho(0)$, where $\rho(H)$ and $\rho(0)$ are the resistivity in the presence and absence of magnetic field, respectively. At 2 K, both TMR and LMR increase with increasing magnetic field and reach a maximum positive value of 8% and 52% around $\mu_0 H_s^c = 3.8$ and $\mu_0 H_m^{ab} = 0.95$ T for $H \parallel c$ and $H \perp c$, respectively [see Fig. 2(c)]. After this maximum value, both MRs drop rapidly and become negative due to the suppression of spin-disorder scattering. TMR and LMR approach saturation values of $\sim -42\%$ and -45% in high fields, respectively, where magnetic moments of Eu^{2+} are completely aligned along the magnetic field direction and become a spin-polarized ferromagnetic (FM) state. However, the positive maximum in TMR and LMR moves to the lower magnetic field as the temperature rises and disappears above T_N. This positive MR below T_N results from the dominance of spin scattering, as typically expected for antiferromagnets [4,31,55]. Interestingly, at $T < T_N$, the positive value of LMR is higher than the TMR due to dominating spin scattering in the *ab* plane. The negative values of TMR and LMR initially increase with increasing temperature up to T_N, then decrease and remain negative up to 40 K. After that, they switch to a small positive value. Above 40 K, values of TMR and LMR are not varying significantly with temperature and remain between 5% and 7%. Furthermore, the TMR and LMR exhibit a cusplike characteristic at low magnetic fields, which is attributed to the WAL phenomenon, as observed in many Eu-based compounds like $EuBiTe_3$ [27] and EuAgAs [4]. The feature of the WAL effect is more prominent in TMR.

E. Hall resistivity

Next, we have performed Hall resistivity (ρ_{xy}) measurements to quantitatively analyze charge carrier densities and mobilities of electrical transport. Figures 5(a) and 5(c) represent the field-dependent $\rho_{xy}(H)$ data at various temperatures 2 to 20 K and 10 to 300 K, respectively. The $\rho_{xy}(H)$ data exhibit a humplike anomaly at $T < 10$ K. This hump is noticeable below T_N and completely disappears above 10 K. This kind of anomaly in $\rho_{xy}(H)$ data has been reported in various magnetic topological systems like GdPtBi [5], CeAlGe [56], Gd_2PdSi_3 [6], $EuAl_4$ [22], and EuPtSi [57], which is attributed

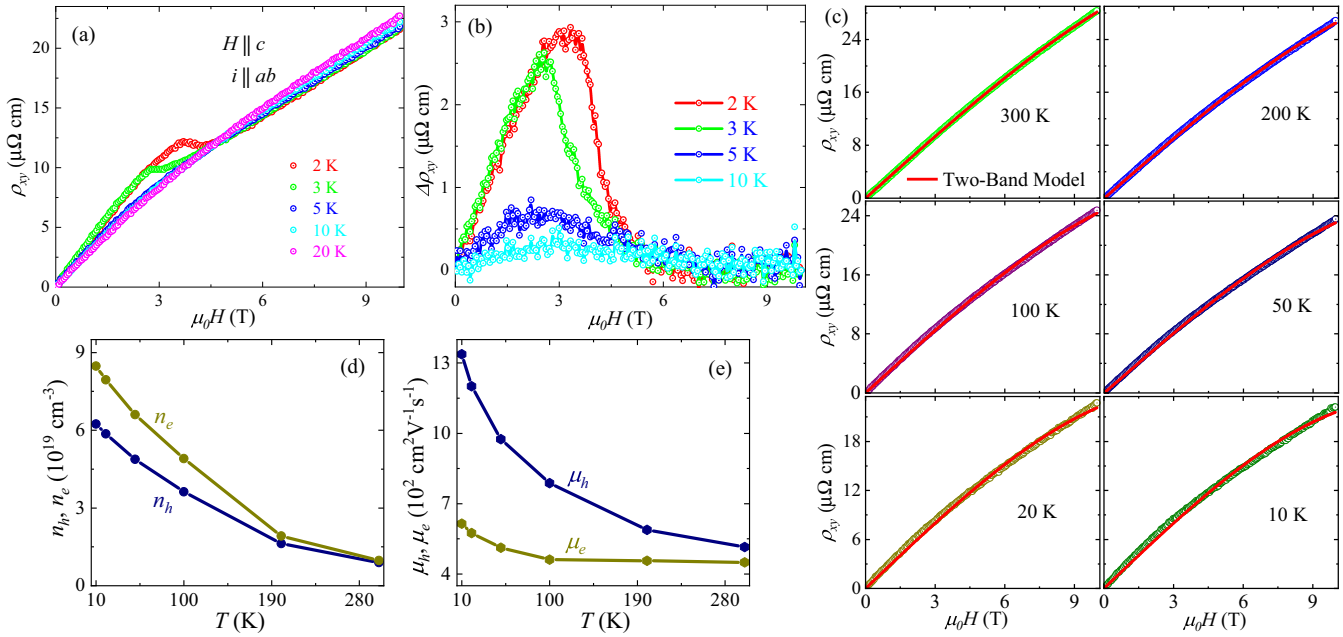

FIG. 5. Panels (a) and (c) present the Hall resistivity as a function of magnetic field at various temperatures from 2 to 300 K. (b) The field dependence of $\Delta\rho_{xy}$ at various temperatures, obtained after subtracting the Hall resistivity at 20 K from the total Hall resistivity at low temperatures (see the text). The red solid line in (c) is the fitting of the two-band model [Eq. (1)]. The temperature variation of (d) carrier densities (n_h, n_e) and (e) mobilities (μ_h, μ_e).

to the THE resulting from topological spin texture. Above 10 K, the $\rho_{xy}(H)$ data show a nonlinear field dependence without any hump, indicating that multiband charge carriers are present in electrical transport of EuAuSb. We employ the semiclassical two-band model to determine charge carrier densities and mobilities. The Hall resistivity based two-band model is given by the expression

$$\rho_{xy} = \frac{H}{e}\frac{\left(n_h\mu_h^2 - n_e\mu_e^2\right) + (n_h - n_e)\mu_e^2\mu_h^2H^2}{(n_e\mu_e + n_h\mu_h)^2 + (n_h - n_e)^2\mu_e^2\mu_h^2H^2}, \quad (1)$$

where n_h (n_e) and μ_h (μ_e) denote the carrier density and mobility of the hole (electron), respectively. The two-band model fitting of $\rho_{xy}(H)$ data in the temperature range of 10–300 K is shown in Fig. 5(c). It is evident from Fig. 5(c) that the two-band model is nicely fitted to the $\rho_{xy}(H)$ data at $T \geqslant 20$ K. At $T = 20$ K, the estimated carrier densities are $n_h = 5.86\times10^{19}$ cm^{-3} and $n_e = 7.94\times10^{19}$ cm^{-3}, which decrease as temperature rises, while mobilities are $\mu_h = 1200$ cm^2 V^{-1} s^{-1} and $\mu_e = 574$ cm^2 V^{-1} s^{-1}. The mobility of electrons remains essentially unchanged with temperature, whereas the mobility of holes continuously decreases with increasing temperatures. The temperature variations of charge carrier densities and mobilities are displayed in Figs. 5(d) and 5(e), respectively. The obtained carrier densities are also comparable to those reported in typical Dirac semimetals ($n \sim 10^{17}$–10^{19} cm^{-3}) [4,58,59], suggesting the semimetallic nature of EuAuSb.

Next, we address the hump anomaly in $\rho_{xy}(H)$. In general, the total Hall resistivity can be expressed as $\rho_{xy} = \rho_{xy}^O + \Delta\rho_{xy}$ for magnetic materials, where ρ_{xy}^O is the ordinary Hall resistivity. $\Delta\rho_{xy}$ refers to anomalous Hall resistivity, which includes the intrinsic terms arising from the spin texture, the Berry curvature due to nontrivial band topology, and the extrinsic terms resulting from side jump and skew scattering [60]. Well above T_N, the ρ_{xy} at $T = 20$ K is well fitted by the two-band model [see Fig. 5(c)], indicating the ordinary Hall component is only present in ρ_{xy} at this temperature; we consider it $\rho_{xy}^O \approx \rho_{xy}(20\text{ K})$. Then, we calculate the hump anomaly using the expression $\Delta\rho_{xy} = \rho_{xy} - \rho'_{xy}(20\text{ K})$, where $\rho'_{xy}(20\text{ K})$ is rescaled to Hall resistivity data at that temperature [2,5]. The obtained $\Delta\rho_{xy}$ is shown in Fig. 5(b) for different temperatures, which is more pronounced below T_N. At 2 K, $\Delta\rho_{xy}$ has maximum value (peak) around 3.4 T. The peak moves towards a lower field and becomes broader with increasing temperature. Further, $\Delta\rho_{xy}$ can also be written as $\Delta\rho_{xy} = \rho_{xy}^A + \rho_{xy}^T$, where ρ_{xy}^A and ρ_{xy}^T are the conventional anomalous Hall resistivity and topological Hall resistivity, respectively. The conventional anomalous Hall resistivity can be either expressed as $S_H\rho_{xx}^2M$ for the dominant intrinsic scattering mechanism (for disordered systems) or $S'_H\rho_{xx}M$ for skew scattering (expected for ultraclean systems), where S_H and S'_H are material-dependent prefactors, and ρ_{xx} and M are field-dependent resistivity and isothermal magnetization [22,24]. Here, both terms $S_H\rho_{xx}^2M$ and $S'_H\rho_{xx}M$ are determined from magnetoresistivity and isothermal magnetization data, as shown in Fig. 6. The term $S_H\rho_{xx}^2M$ gives slightly better proximity to the hump anomaly than $S'_H\rho_{xx}M$. We are assuming that ρ_{xy}^O at 2 K is equal to the rescaled $\rho_{xy}(20\text{ K})$ data (see Fig. 6). It is clear from Fig. 6 that the term $\rho_{xy}^O + S_H\rho_{xx}^2M$ does not reproduce the total Hall resistivity, indicating the topological component ρ_{xy}^T also contributes to the hump anomaly. The calculated topological Hall component is displayed in the inset of Fig. 6, which has the maximum around 3 T.

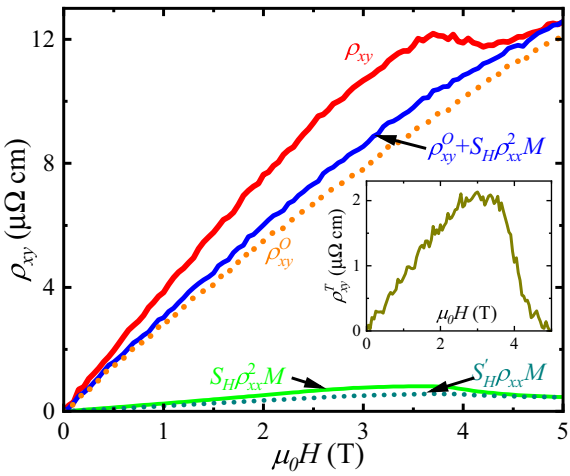

FIG. 6. The red and blue solid lines present field-dependent observed ρ_{xy} and calculated $\rho^O_{xy} + S_H\rho^2_{xx}M$, respectively. The ordinary term is assumed to $\rho^O_{xy}(2\text{ K}) \approx \rho_{xy}(20\text{ K})$ (dotted orange line) after rescaling. The solid green and dotted cyan line display $\rho^2_{xx}M$ and $\rho_{xx}M$ as a function of field, respectively. The inset shows field dependence of topological Hall component. All these results are based on the data of 2 K.

F. Electronic structure

EuAuSb crystallizes in a hexagonal structure with the centrosymmetric space group $P6_3/mmc$ (No. 194), as shown in Fig. 7(a). The structural arrangement of EuAuSb involves six atoms within the unit cell. In the structure, Au and Sb collaborate to form parallel layers resembling a honeycomb arrangement. Within each honeycomb layer, distinct atoms occupy the A and B sites. As a result of this diverse atom arrangement, these layers stack parallel to the z direction. The Eu layer is sandwiched between two neighboring Au-Sb layers, which maintain the inversion symmetry throughout the structure. In the unit cell, Au (Sb) resides at position $2d$ ($2c$), while Eu occupies position $2a$ according to the Wyckoff diagram. The lattice symmetry group is defined by several generators: a threefold rotation (C_{3z}), inversion (P), a twofold rotation (C_{2y}), a twofold screw rotation ($S_{2z} = \{C_{2z}|00\frac{1}{2}\}$) with a half-translation along the z direction and mirror symmetries M_z, M_x, and $\widetilde{M}_y$, where $\widetilde{M}_y = \{M_y|00\frac{1}{2}\}$ represents a glide mirror operation. To explore potential magnetic arrangement of our investigated compound, we analyzed

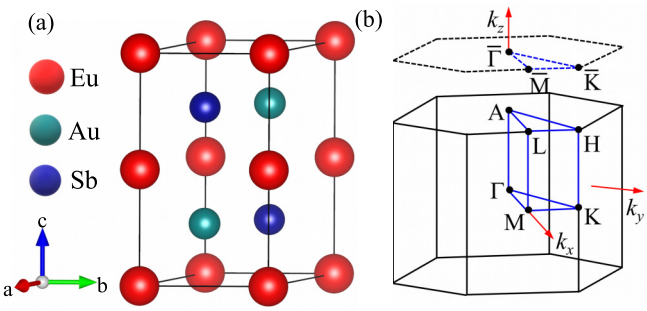

FIG. 7. (a) The crystal structure of EuAuSb. (b) The irreducible Brillouin zone of the bulk along with the (001) projected surface.

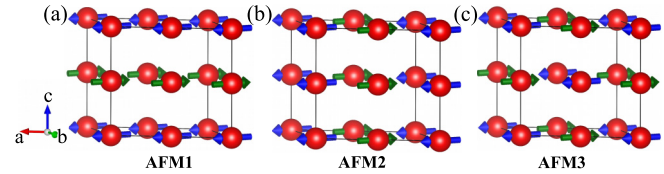

FIG. 8. (a)–(c) AFM configurations for 2×1×1 supercell with Eu spins. Here, AFM1, AFM2, and AFM3 are *A*-, *C*-, and *G*-type AFM, respectively. Blue and green arrows denote the spin-up and spin-down, respectively.

distinct AFM configurations using a 2×1×1 supercell. These possible magnetic configurations are depicted in Fig. 8. The computed ground state energies for each configuration are listed in Table I. The results in Table I indicate that the AFM2 configuration demonstrates the lowest energy, where the AFM2 configuration showcases AFM coupling along the a axis, while FM coupling occurs along the b and c axes. However, the calculated energy difference between AFM1 and AFM2 is very small (0.59 meV), so we have computed the electronic band structure for both cases. The calculated electronic band structures for both cases are found similar to each other, which is shown in Fig. 9. In the absence of SOC, both cases show Dirac-like crossing points along the $k_z = 0$ plane. The presence of SOC reveals the fourfold degeneracy at high-symmetry point A in both configurations. We can see that both configurations exhibit similar topological features. Furthermore, our field- and temperature-dependent magnetization data suggest A-type AFM order due to lower values of magnetization along the c axis compared to the ab plane. The discrepancy between DFT and experimental results may be due to the temperature effect, as DFT calculations are valid at 0 K. Thus, we carried on with all DFT calculations using our experimentally suggested magnetic structure (i.e., the AFM1 case). To further analyze our compound, we have computed the electronic band structure and surface states for the lower cell (1×1×1) of the AFM1 case. To provide additional validation for the spin orientations in the AFM1 case, we calculated the ground state energies for various spin alignments, including [001], [010], [100], [011], [101], [110], and [111]. Table II displays the computed discrepancies in the ground state energies of different spin configurations. Notably, the [110] spin configuration demonstrates the lowest ground state energy, which is consistent with our experimental findings.

To depict the characteristics of Eu-f states, we calculated the total density of states (DOS) and the projected density of states, as shown in the Fig. 10(a). In both spin-up and spin-down channels, the valence band is predominantly governed by Eu-f states, with minimal DOS observed at the Fermi level, which confirms the semimetallic nature of the compound. Furthermore, we explored the electronic band

TABLE I. Calculated energies of different AFM configurations (in meV) with the reference energy considered to be 0 meV.

Configuration	AFM1	AFM2	AFM3
Energy (meV)	0.59	0.00	0.88

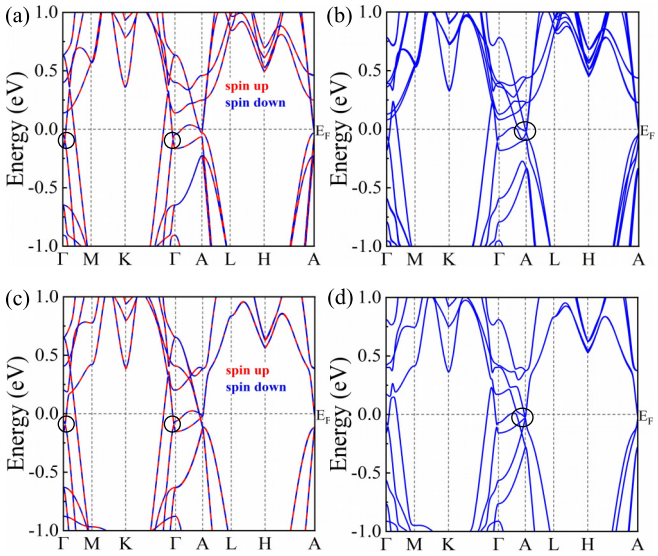

FIG. 9. Electronic band structure along high-symmetry points without SOC for (a) AFM1 and (c) AFM2 case. Electronic band structure with SOC along [110] direction for (b) AFM1 and (d) AFM2 case.

structure properties. As depicted in Fig. 10(b), the electronic band structure is illustrated for both spin-up (in red) and spin-down (in blue) channels. The electronic band structure holds significant interest due to the presence of Dirac-like linearized points in close proximity to the Fermi level along the M-Γ-K path. This phenomenon potentially hints at the existence of a nodal line. To confirm the presence of a nodal line, we have done the symmetry analysis. Our calculations of irreducible representations [61] indicate that the two bands [see Fig. 10(c)] can be attributed to the Γ_2^- and Γ_1^+ irreducible representations, respectively. As a consequence of their differing parity, we deduce the occurrence of band inversion, ensuring the presence of a nodal line.

Figure 11(a) illustrates the surface states with Au termination. The plots depict both the nodal line and a drumhead surface state connecting crossing points along M-Γ and Γ-K. The nodal line is observable in the bulk band structure, positioned slightly below the Fermi level. To validate the nodal line depicted in Fig. 11(a), we have performed the energy gap plane calculations. The continuous Γ-centered ring visible in Fig. 11(b) ensures the presence of the nodal ring in the $k_z = 0$ plane, which remains protected by mirror symmetry (M_z).

We included SOC to confirm the nontrivial topology here since the analyzed system has crossing points. Figure 10(d) depicts the electronic band structure with SOC. We have done a thorough analysis of the band crossings at high-symmetry point A in the presence of SOC. Due to the presence of nonsymmorphic and inversion symmetries in the space group, the

TABLE II. Calculated energies of different spin configurations in AFM1 state with the reference energy considered to be 0 μeV.

Configuration	[001]	[010]	[100]	[011]	[101]	[110]	[111]
Energy (μeV)	181.08	0.01	0.49	90.45	90.62	0.00	60.29

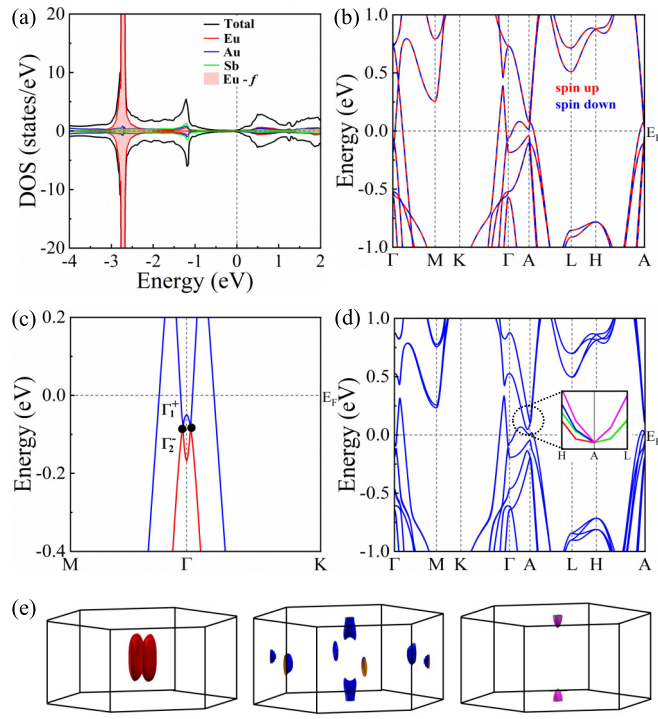

FIG. 10. (a) Total and projected density of states of EuAuSb. (b) Electronic band structure along high-symmetry points without SOC. (c) Electronic band structure along M-Γ-K path without SOC. (d) Electronic band structure with SOC along [110] direction. Here, inset shows the band structure along H-A-L path with a Dirac point at A. (e) The Fermi surfaces, i.e., hole and electron pockets with SOC.

A point hosts fourfold degeneracy (known as the Dirac point). The AFM topological material EuAgAs [4], EuAuAs [31], which possesses both inversion and effective time-reversal symmetry, is analogous to the system under investigation. This observation prompts us to undertake calculations of the Z_2 invariants, yielding values of (1;0 0 0). The presence of the Dirac points along the Γ-A path and the determined Z_2 invariants collectively serve as compelling evidence to designate EuAuSb as a strong nontrivial topological material. Additionally, we have calculated the Fermi surfaces, which are shown in Fig. 10(e). We can see that a large hole pocket and two small electron pockets are present at the Fermi level, which is in good accordance with the experimentally measured Hall resistivity data.

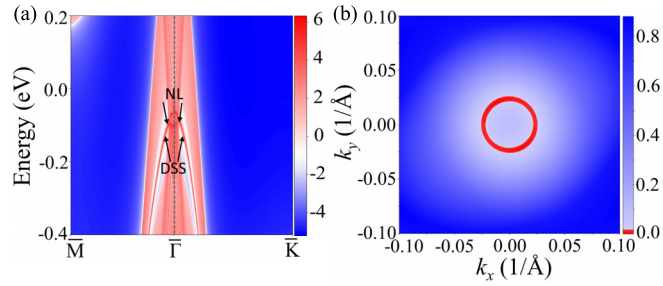

FIG. 11. (a) The surface states with Au termination and (b) the corresponding energy gap plane in the $k_z = 0$ plane.

IV. CONCLUSIONS

In conclusion, we have presented a systematic study of the EuAuSb single crystal using the magnetization, heat capacity, magnetotransport measurements, and electronic band structure calculations. The powder XRD data reveal that EuAuSb crystallizes in a hexagonal structure with space group $P6_3/mmc$. The compound EuAuSb undergoes an AFM ordering below $T_N = 3.3$ K, verified through magnetic susceptibility, heat capacity, and electrical resistivity measurements. The $\rho(T)$ shows a metallic behavior, following a sharp upturn below 35 K, which is suppressed under applied magnetic field. Below T_N, the TMR and LMR of EuAuSb exhibit a positive value in low field up to $\mu_0 H_s^c = 3.8$ and $\mu_0 H_m^{ab} = 0.95$ T, respectively, after which both MRs drop rapidly to become negative and saturate in high fields. Above T_N, TMR and LMR become negative in the whole measured magnetic field range until 40 K; after that, they switch to a small positive value and remain up to 300 K. The Hall resistivity data exhibit a hump anomaly below T_N, which is attributed to the THE. The semiclassical two-band model nicely fits the Hall resistivity data above 10 K, suggesting both electron and hole carriers contribute to the electrical transport. The theoretical calculations unveiled the emergence of a nodal line in the absence of SOC. This nodal line is positioned just below the Fermi level and is protected by the mirror symmetry. Considering the inclusion of SOC, EuAuSb emerges as a fresh contender in the realm of AFM topological materials.

ACKNOWLEDGMENTS

We acknowledge IIT Kanpur and the Department of Science and Technology, India [Order No. DST/NM/TUE/QM-06/2019 (G)], for financial support. We thank S. N. Sarangi for the magnetic measurements. J.S. and V.K. acknowledge the National Supercomputing Mission (NSM) for providing computing resources of "PARAM SEVA" at IIT, Hyderabad. V.K. would like to acknowledge DST-FIST (Grant No. SR/FST/PSI-215/2016) for financial support. J.S. and S.B. were supported through a CSIR fellowship.

[1] N. Kanazawa, Y. Onose, T. Arima, D. Okuyama, K. Ohoyama, S. Wakimoto, K. Kakurai, S. Ishiwata, and Y. Tokura, Large topological Hall effect in a short-period helimagnet MnGe, Phys. Rev. Lett. **106**, 156603 (2011).

[2] H. Zhang, Y. L. Zhu, Y. Qiu, W. Tian, H. B. Cao, Z. Q. Mao, and X. Ke, Field-induced magnetic phase transitions and the resultant giant anomalous Hall effect in the antiferromagnetic half-Heusler compound DyPtBi, Phys. Rev. B **102**, 094424 (2020).

[3] D. Ram, S. Malick, Z. Hossain, and D. Kaczorowski, Magnetic, thermodynamic, and magnetotransport properties of CeGaGe and PrGaGe single crystals, Phys. Rev. B **108**, 024428 (2023).

[4] A. Laha, R. Singha, S. Mardanya, B. Singh, A. Agarwal, P. Mandal, and Z. Hossain, Topological Hall effect in the antiferromagnetic Dirac semimetal EuAgAs, Phys. Rev. B **103**, L241112 (2021).

[5] T. Suzuki, R. Chisnell, A. Devarakonda, Y.-T. Liu, W. Feng, D. Xiao, J. W. Lynn, and J. G. Checkelsky, Large anomalous Hall effect in a half-Heusler antiferromagnet, Nat. Phys. **12**, 1119 (2016).

[6] T. Kurumaji, T. Nakajima, M. Hirschberger, A. Kikkawa, Y. Yamasaki, H. Sagayama, H. Nakao, Y. Taguchi, T.-H. Arima, and Y. Tokuras, Skyrmion lattice with a giant topological Hall effect in a frustrated triangular-lattice magnet, Science **365**, 914 (2019).

[7] E. Liu, Y. Sun, N. Kumar, L. Muechler, A. Sun, L. Jiao, S.-Y. Yang, D. Liu, A. Liang, Q. Xu, J. Kroder, V. Süß, H. Borrmann, C. Shekhar, Z. Wang, C. Xi, W. Wang, W. Schnelle, S. Wirth, Y. Chen *et al.*, Giant anomalous Hall effect in a ferromagnetic kagome-lattice semimetal, Nat. Phys. **14**, 1125 (2018).

[8] R. Singha, S. Roy, A. Pariari, B. Satpati, and P. Mandal, Magnetotransport properties and giant anomalous Hall angle in the half-Heusler compound TbPtBi, Phys. Rev. B **99**, 035110 (2019).

[9] B. Meng, H. Wu, Y. Qiu, C. Wang, Y. Liu, Z. Xia, S. Yuan, H. Chang, and Z. Tian, Large anomalous Hall effect in ferromagnetic Weyl semimetal candidate PrAlGe, APL Mater. **7**, 051110 (2019).

[10] Y. Shiomi, N. Kanazawa, K. Shibata, Y. Onose, and Y. Tokura, Topological Nernst effect in a three-dimensional skyrmion-lattice phase, Phys. Rev. B **88**, 064409 (2013).

[11] Y. Xu, L. Das, J. Z. Ma, C. J. Yi, S. M. Nie, Y. G. Shi, A. Tiwari, S. S. Tsirkin, T. Neupert, M. Medarde, M. Shi, J. Chang, and T. Shang, Unconventional transverse transport above and below the magnetic transition temperature in Weyl semimetal $EuCd_2As_2$, Phys. Rev. Lett. **126**, 076602 (2021).

[12] M. Hirschberger, S. Kushwaha, Z. Wang, Q. Gibson, S. Liang, C. Belvin, B. A. Bernevig, R. J. Cava, and N. P. Ong, The chiral anomaly and thermopower of Weyl fermions in the half-Heusler GdPtBi, Nat. Mater. **15**, 1161 (2016).

[13] S. Borisenko, D. Evtushinsky, Q. Gibson, A. Yaresko, K. Koepernik, T. Kim, M. Ali, J. van den Brink, M. Hoesch, A. Fedorov, E. Haubold, Y. Kushnirenko, I. Soldatov, R. Schäfer, and R. J. Cava, Time-reversal symmetry breaking type-II Weyl state in $YbMnBi_2$, Nat. Commun. **10**, 3424 (2019).

[14] Y. Du, B. Wan, D. Wang, L. Sheng, C.-G. Duan, and X. Wan, Dirac and Weyl semimetal in *XY*Bi (X = Ba, Eu; Y = Cu, Ag and Au), Sci. Rep. **5**, 14423 (2015).

[15] K. Tsuruda, K. Nakagawa, M. Ochi, K. Kuroki, M. Tokunaga, H. Murakawa, N. Hanasaki, and H. Sakai, Enhancing thermopower and Nernst signal of high-mobility Dirac carriers by Fermi level tuning in the layered magnet $EuMnBi_2$, Adv. Funct. Mater. **31**, 2102275 (2021).

[16] R. Yu, W. Zhang, H.-J. Zhang, S.-C. Zhang, X. Dai, and Z. Fang, Quantized anomalous Hall effect in magnetic topological insulators, Science **329**, 61 (2010).

[17] Y. Deng, Y. Yu, M. Z. Shi, Z. Guo, Z. Xu, J. Wang, X. H. Chen, and Y. Zhang, Quantum anomalous Hall effect in intrinsic magnetic topological insulator $MnBi_2Te_4$, Science **367**, 895 (2020).

[18] X.-L. Qi, Y.-S. Wu, and S.-C. Zhang, Topological quantization of the spin Hall effect in two-dimensional paramagnetic semiconductors, Phys. Rev. B **74**, 085308 (2006).

[19] Y. Zhang, K. Deng, X. Zhang, M. Wang, Y. Wang, C. Liu, J.-W. Mei, S. Kumar, E. F. Schwier, K. Shimada, C. Chen, and B. Shen, In-plane antiferromagnetic moments and magnetic polaron in the axion topological insulator candidate $EuIn_2As_2$, Phys. Rev. B **101**, 205126 (2020).

[20] R. Li, J. Wang, X.-L. Qi, and S.-C. Zhang, Dynamical axion field in topological magnetic insulators, Nat. Phys. **6**, 284 (2010).

[21] S. Regmi, M. M. Hosen, B. Ghosh, B. Singh, G. Dhakal, C. Sims, B. Wang, F. Kabir, K. Dimitri, Y. Liu, A. Agarwal, H. Lin, D. Kaczorowski, A. Bansil, and M. Neupane, Temperature-dependent electronic structure in a higher-order topological insulator candidate $EuIn_2As_2$, Phys. Rev. B **102**, 165153 (2020).

[22] T. Shang, Y. Xu, D. J. Gawryluk, J. Z. Ma, T. Shiroka, M. Shi, and E. Pomjakushina, Anomalous Hall resistivity and possible topological Hall effect in the $EuAl_4$ antiferromagnet, Phys. Rev. B **103**, L020405 (2021).

[23] C. Yi, S. Yang, M. Yang, L. Wang, Y. Matsushita, S. Miao, Y. Jiao, J. Cheng, Y. Li, K. Yamaura, Y. Shi, and J. Luo, Large negative magnetoresistance of a nearly Dirac material: Layered antimonide $EuMnSb_2$, Phys. Rev. B **96**, 205103 (2017).

[24] J. M. Moya, S. Lei, E. M. Clements, C. S. Kengle, S. Sun, K. Allen, Q. Li, Y. Y. Peng, A. A. Husain, M. Mitrano, M. J. Krogstad, R. Osborn, A. B. Puthirath, S. Chi, L. Debeer-Schmitt, J. Gaudet, P. Abbamonte, J. W. Lynn, and E. Morosan, Incommensurate magnetic orders and topological Hall effect in the square-net centrosymmetric $EuGa_2Al_2$ system, Phys. Rev. Mater. **6**, 074201 (2022).

[25] N. H. Jo, B. Kuthanazhi, Y. Wu, E. Timmons, T.-H. Kim, L. Zhou, L.-L. Wang, B. G. Ueland, A. Palasyuk, D. H. Ryan, R. J. McQueeney, K. Lee, B. Schrunk, A. A. Burkov, R. Prozorov, S. L. Bud'ko, A. Kaminski, and P. C. Canfield, Manipulating magnetism in the topological semimetal $EuCd_2As_2$, Phys. Rev. B **101**, 140402(R) (2020).

[26] H. Masuda, H. Sakai, M. Tokunaga, Y. Yamasaki, A. Miyake, J. Shiogai, S. Nakamura, S. Awaji, A. Tsukazaki, H. Nakao, Y. Murakami, T. hisa Arima, Y. Tokura, and S. Ishiwata, Quantum Hall effect in a bulk antiferromagnet $EuMnBi_2$ with magnetically confined two-dimensional Dirac fermions, Sci. Adv. **2**, e1501117 (2016).

[27] W. Shon, J.-S. Rhyee, Y. Jin, and S.-J. Kim, Magnetic polaron and unconventional magnetotransport properties of the single-crystalline compound $EuBiTe_3$, Phys. Rev. B **100**, 024433 (2019).

[28] E. Cheng, W. Xia, X. Shi, H. Fang, C. Wang, C. Xi, S. Xu, D. C. Peets, L. Wang, H. Su, L. Pi, W. Ren, X. Wang, N. Yu, Y. Chen, W. Zhao, Z. Liu, Y. Guo, and S. Li, Magnetism-induced topological transition in $EuAs_3$, Nat. Commun. **12**, 6970 (2021).

[29] A. H. Mayo, H. Takahashi, M. S. Bahramy, A. Nomoto, H. Sakai, and S. Ishiwata, Magnetic generation and switching of topological quantum phases in a trivial semimetal α-EuP_3, Phys. Rev. X **12**, 011033 (2022).

[30] H. Takahashi, K. Aono, Y. Nambu, R. Kiyanagi, T. Nomoto, M. Sakano, K. Ishizaka, R. Arita, and S. Ishiwata, Competing spin modulations in the magnetically frustrated semimetal EuCuSb, Phys. Rev. B **102**, 174425 (2020).

[31] S. Malick, J. Singh, A. Laha, V. Kanchana, Z. Hossain, and D. Kaczorowski, Electronic structure and physical properties of EuAuAs single crystal, Phys. Rev. B **105**, 045103 (2022).

[32] H. Takahashi, K. Akiba, M. Takahashi, A. H. Mayo, M. Ochi, T. C. Kobayashi, and S. Ishiwata, Superconductivity in a magnetic Rashba semimetal EuAuBi, J. Phys. Soc. Jpn. **92**, 013701 (2023).

[33] P. Hohenberg and W. Kohn, Inhomogeneous electron gas, Phys. Rev. **136**, B864 (1964).

[34] W. Kohn and L. J. Sham, Self-consistent equations including exchange and correlation effects, Phys. Rev. **140**, A1133 (1965).

[35] P. E. Blöchl, Projector augmented-wave method, Phys. Rev. B **50**, 17953 (1994).

[36] G. Kresse and J. Furthmüller, Efficient iterative schemes for *ab initio* total-energy calculations using a plane-wave basis set, Phys. Rev. B **54**, 11169 (1996).

[37] G. Kresse and D. Joubert, From ultrasoft pseudopotentials to the projector augmented-wave method, Phys. Rev. B **59**, 1758 (1999).

[38] J. P. Perdew, K. Burke, and M. Ernzerhof, Generalized gradient approximation made simple, Phys. Rev. Lett. **77**, 3865 (1996).

[39] X. Wan, J. Dong, and S. Y. Savrasov, Mechanism of magnetic exchange interactions in europium monochalcogenides, Phys. Rev. B **83**, 205201 (2011).

[40] J. Kuneš and R. Laskowski, Magnetic ground state and Fermi surface of bcc Eu, Phys. Rev. B **70**, 174415 (2004).

[41] H. J. Monkhorst and J. D. Pack, Special points for Brillouin-zone integrations, Phys. Rev. B **13**, 5188 (1976).

[42] G. Pizzi, V. Vitale, R. Arita, S. Blügel, F. Freimuth, G. Géranton, M. Gibertini, D. Gresch, C. Johnson, T. Koretsune, J. Ibañez-Azpiroz, H. Lee, J.-M. Lihm, D. Marchand, A. Marrazzo, Y. Mokrousov, J. I. Mustafa, Y. Nohara, Y. Nomura, L. Paulatto *et al.*, Wannier90 as a community code: New features and applications, J. Phys.: Condens. Matter **32**, 165902 (2020).

[43] M. P. L. Sancho, J. M. Lopez Sancho, J. M. L. Sancho, and J. Rubio, Highly convergent schemes for the calculation of bulk and surface Green functions, J. Phys. F **15**, 851 (1985).

[44] Q. Wu, S. Zhang, H.-F. Song, M. Troyer, and A. A. Soluyanov, WannierTools: An open-source software package for novel topological materials, Comput. Phys. Commun. **224**, 405 (2018).

[45] H. Suzuki, T. Yamaguchi, K. Katoh, and M. Kasaya, Physical properties of ternary rare earth compounds RPt(Au)Sb, Phys. B: Condens. Matter **186-188**, 390 (1993).

[46] C. Tomuschat and H.-U. Schuster, ABX-Verbindungen mit modifizierter Ni_2 In-Struktur/ABX-Compounds with a modified Ni_2 In structure, Z. Naturforsch. B **36**, 1193 (1981).

[47] T. Mishra, I. Schellenberg, M. Eul, and R. Pöttgen, Structure and properties of Eu*T*Sb (T = Cu, Pd, Ag, Pt, Au) and YbIrSb, Z. Kristallogr. **226**, 590 (2011).

[48] D. Ram, J. Singh, M. K. Hooda, O. Pavlosiuk, V. Kanchana, Z. Hossain, and D. Kaczorowski, Electronic structure and physical properties of the candidate topological material GdAgGe, Phys. Rev. B **107**, 085137 (2023).

[49] V. K. Anand, A. Thamizhavel, S. Ramakrishnan, and Z. Hossain, Complex magnetic order in $Pr_2Pd_3Ge_5$: A single crystal study, J. Phys.: Condens. Matter **24**, 456003 (2012).

[50] D. Ram, J. Singh, M. K. Hooda, K. Singh, V. Kanchana, D. Kaczorowski, and Z. Hossain, Multiple magnetic transitions, metamagnetism, and large magnetoresistance in GdAuGe single crystals, Phys. Rev. B **108**, 235107 (2023).

[51] J. Tong, J. Parry, Q. Tao, G.-H. Cao, Z.-A. Xu, and H. Zeng, Magnetic properties of EuCuAs single crystal, J. Alloys Compd. **602**, 26 (2014).

[52] A. Bauer, A. Senyshyn, R. Bozhanova, W. Simeth, C. Franz, S. Gottlieb-Schönmeyer, M. Meven, T. E. Schrader, and C. Pfleiderer, Magnetic properties of the noncentrosymmetric tetragonal antiferromagnet $EuPtSi_3$, Phys. Rev. Mater. **6**, 034406 (2022).

[53] U. B. Paramanik, R. Prasad, C. Geibel, and Z. Hossain, Itinerant and local-moment magnetism in $EuCr_2As_2$ single crystals, Phys. Rev. B **89**, 144423 (2014).

[54] J. A. Blanco, D. Gignoux, and D. Schmitt, Specific heat in some gadolinium compounds. II. Theoretical model, Phys. Rev. B **43**, 13145 (1991).

[55] T. Toliński and D. Kaczorowski, Magnetic properties of the putative higher-order topological insulator $EuIn_2As_2$, SciPost Phys. Proc. **11**, 005 (2023).

[56] P. Puphal, V. Pomjakushin, N. Kanazawa, V. Ukleev, D. J. Gawryluk, J. Ma, M. Naamneh, N. C. Plumb, L. Keller, R. Cubitt, E. Pomjakushina, and J. S. White, Topological magnetic phase in the candidate Weyl semimetal CeAlGe, Phys. Rev. Lett. **124**, 017202 (2020).

[57] M. Kakihana, D. Aoki, A. Nakamura, F. Honda, M. Nakashima, Y. Amako, S. Nakamura, T. Sakakibara, M. Hedo, T. Nakama, and Y. Ōnuki, Giant Hall resistivity and magnetoresistance in cubic chiral antiferromagnet EuPtSi, J. Phys. Soc. Jpn. **87**, 023701 (2018).

[58] L. Li, K. Wang, D. Graf, L. Wang, A. Wang, and C. Petrovic, Electron-hole asymmetry, Dirac fermions, and quantum magnetoresistance in $BaMnBi_2$, Phys. Rev. B **93**, 115141 (2016).

[59] Z. Hu, J. Koo, Y. Hu, Q. Wang, M. Abeykoon, D. Graf, Y. Liu, H. Lei, J. Ma, M. Shi, B. Yan, and C. Petrovic, Topological Dirac semimetal BaAuSb, Phys. Rev. Res. **5**, 013079 (2023).

[60] N. Nagaosa, J. Sinova, S. Onoda, A. H. MacDonald, and N. P. Ong, Anomalous Hall effect, Rev. Mod. Phys. **82**, 1539 (2010).

[61] J. Gao, Q. Wu, C. Persson, and Z. Wang, Irvsp: To obtain irreducible representations of electronic states in the VASP, Comput. Phys. Commun. **261**, 107760 (2021).